Int. J. Heat Mass Transfer. Vol. 36, No. 16, pp. 4049–4066, 1993
Printed in Great Britain

0017–9310/93 $6.00+0.00

Heat transfer to a horizontal disc using a buoyancy-induced jet

SANGEETA KOHLI and J. SRINIVASAN
Department of Mechanical Engineering, Indian Institute of Science, Bangalore 560 012, India

and

H. S. MUKUNDA
Department of Aerospace Engineering, Indian Institute of Science, Bangalore 560 012, India

(*Received* 6 *May* 1992)

Abstract—A study of the buoyancy-induced flow from a hot vertical tube impinging on a cold horizontal disc has been carried out. This geometry is analogous to a single pan biomass stove, with a vertical tube followed by a horizontal radial diffuser. Flow visualization experiments have been conducted to observe the flow in the diffuser. These visualizations show a recirculation zone at the entrance of the diffuser whose size depends on the diffuser spacing. A numerical simulation of the system has been carried out using a finite difference technique to study the dependence of fluid flow and heat transfer on Grashof number and the geometrical parameters. The details of the buoyancy induced flow structure are elucidated. The size of recirculation zone and the flow pattern in the diffuser predicted by the calculations is similar to those observed in experiments. The spacing between the diffuser discs is found to have a strong influence on the flow pattern, mass flow and heat transfer to the horizontal disc. The outer radius of the diffuser mainly affects the total heat transfer to the disc.

1. INTRODUCTION

BUOYANCY-INDUCED flow through a vertical channel has been investigated extensively in literature mainly due to its relevance to electronic cooling [1–4] and solar applications [5]. Natural convection flow through vertical tubes has also received some attention [6–9]. The main interest in these investigations has been cooling of the duct walls. While the flow through the duct takes away heat from the walls, the hot fluid coming out of the duct may be considered as a source of heat and used for heating a surface. As the stream of hot fluid emerges from the duct with some momentum, it can be considered as a *buoyancy-induced jet*.

The hot jet emerging from a vertical duct may be used for heating a horizontal surface by impingement. Figure 1 shows a vertical heated tube acting as a source of a buoyancy-induced jet, and the jet impinging on a horizontal surface. Such a configuration is encountered in a certain class of biomass stoves [10], where the hot flue gases from the combustion chamber impinge on the bottom of a vessel. The vessel is supported on a disc as shown in Fig. 1, so that the passage of flue gases after impingement forms a radial diffuser.

The impingement of the jet on the surface to be heated causes the formation of a stagnation zone, increasing the pressure at the exit of the tube and hence influences the flow in the tube. The presence of the radial diffuser adds to the resistance to the flow through the system and affects the heat transfer to the vessel. The sharp bend in the flow at the inlet of the diffuser also adds to the complexity of the flow. Thus there is a coupling between fluid flow and heat transfer through a vertical duct, a stagnation zone and a radial diffuser.

The combination of these elements, namely the buoyant impinging jet and the radial diffuser flow presents an interesting and complex situation that

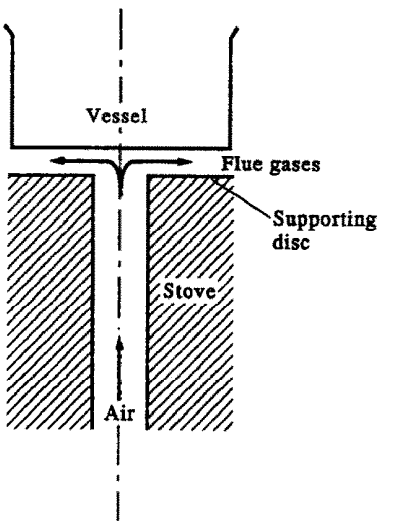

FIG. 1. Geometry of a simple biomass stove.

has not been considered so far. The present work, therefore, deals with the study of such a configuration (shown in Fig. 1) in which the source of the buoyancy-induced jet is a vertical tube maintained at a constant temperature. The top surface of the diffuser is a disc maintained at a constant temperature lower than that of the duct wall. The bottom surface is an adiabatic disc. Flow visualization in the radial diffuser has been carried out to observe the effect of spacing between the discs on the flow pattern qualitatively. To obtain quantitative information on the flow field and heat transfer, numerical simulation of the flow has been carried out. In contrast to the investigations on flow through an open tube, the present simulation involves solution of full Navier–Stokes equations without the boundary layer and Boussinesq approximations. A qualitative comparison between the observed and the simulated flow patterns is presented. The dependence of the mass flow rates and heat fluxes on the geometric and other parameters is investigated.

2. FLOW VISUALIZATION

The experimental set-up consisted of a vertical mild steel tube of 40 mm diameter and 300 mm height. A horizontal disc fixed to the upper end of the tube formed the bottom surface of the diffuser. The vessel, forming the upper surface of the diffuser was kept at the desired distance from the tube by means of guides and a chord and pulley arrangement. A schematic of the experimental setup is shown in Fig. 2.

The vertical tube was heated electrically by means of a ceramic heater surrounding the tube. Heat loss to the ambient was minimized using alumino-silicate insulation around the heater. The wall temperatures on the tube surface were measured using chromel-

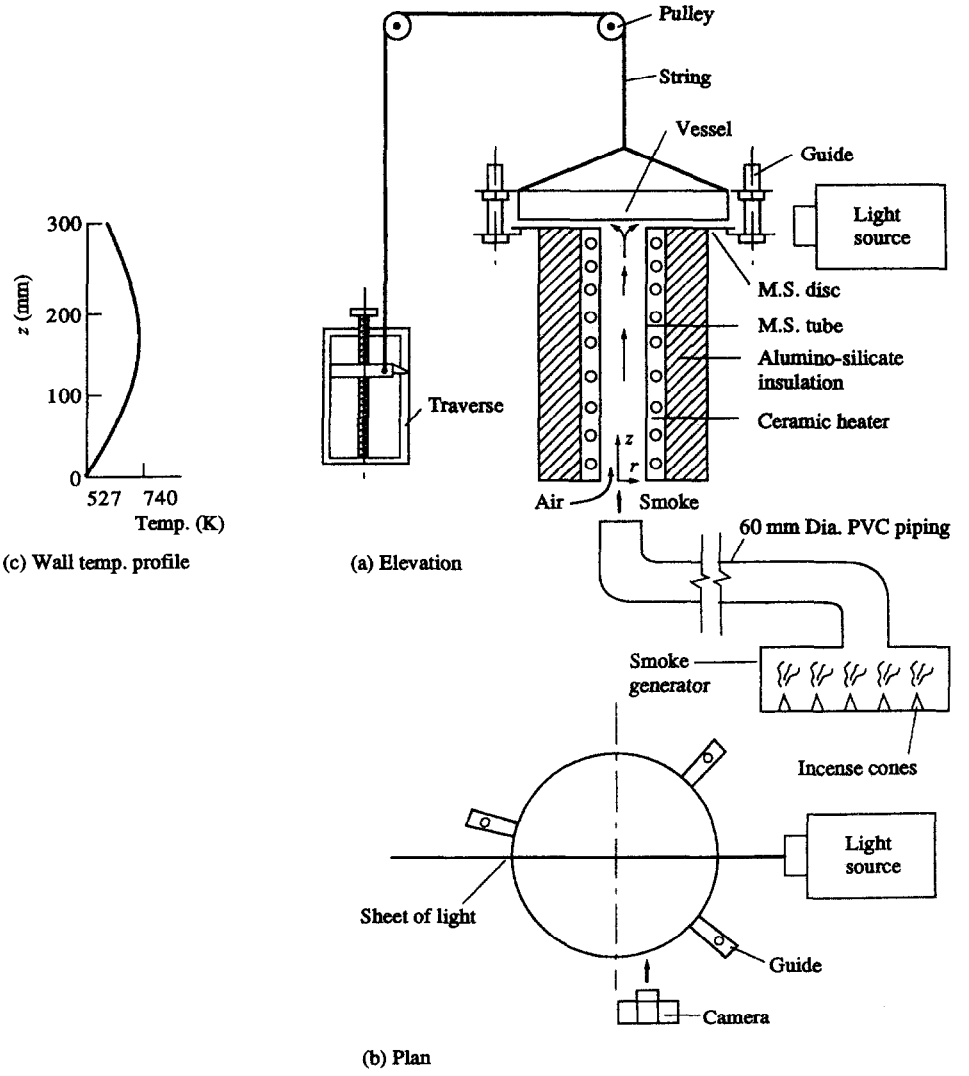

FIG. 2. Schematic of the experimental set-up.

alumel thermocouples fixed on the outer surface of the tube at intervals of 20 mm along the length of the tube.

White smoke was used for visualizing the flow in the diffuser. Considerable experimentation was required before finalizing the methodology of flow visualization using smoke. Smoke was generated in an enclosure by burning incense cones. It was made *neutrally buoyant* by passing it through sufficiently long PVC piping. A PVC pipe 60 mm in diameter and 3 m long was sufficient to obtain a neutrally buoyant smoke. The smoke so generated was released at the inlet of the tube. Due to the suction caused by the heating of the tube, the smoke was carried up along with the flow of air. A sheet of light obtained by using a slit of 3 mm width in a slide projector was used to illuminate the flow field in one axisymmetric (r–z) plane of the diffuser. The flow was photographed by viewing the flow from a direction perpendicular to the light beam (Fig. 2(b)).

The heater was supplied with a steady power of 500 W. The measured wall temperatures reached a steady value in about 10 h. The average tube wall temperature attained was 695 K while the top disc reached a temperature of 397 K. The spacing between the diffuser discs was varied from 5 mm to 12 mm and the flow patterns were photographed.

The results of the flow visualization are presented in the photographs shown in Figs. 3(a)–(h). As seen in Fig. 3(a), at a low spacing of 5 mm, the recirculation region formed due to separation of flow at the bend is quite small. As the spacing is increased, the recirculation region grows in size, as seen in Figs. 3(b)–(e). In all the above cases, the flow was observed to be *steady, laminar and axisymmetric*. However, at spacings beyond 9 mm, the flow was observed to be unsteady and multiple patterns were observed. Figures 3(f) and (g) show two of the patterns observed for a spacing of 10 mm. It can be seen that for spacings higher than 9 mm a second recirculation region is formed at the top disc, downstream of the recirculation region at the bend (Figs. 3(g) and (h)). However, the second recirculation region was highly unstable. It appeared only intermittently and was seen to move downstream with the flow. At certain instants, when no second recirculation zone was seen, the flow pattern was similar to that predicted by the steady state simulation, described later (Fig. 3(f)).

3. NUMERICAL SIMULATION

As shown in Fig. 1, the flow passage comprises a vertical tube followed by a horizontal radial diffuser. The flow is axisymmetric and hence the computational domain is a two dimensional region as shown in Fig. 4. The equations governing the conservation of mass, momentum and energy have been solved in this domain. The flow is assumed to be laminar on the basis of observation during flow visualization.

The use of the Boussinesq approximation for density variation is common in natural convection problems. This approximation is, however, valid for temperature differences less than about 30°C [11]. In the case of biomass stoves the temperature differences are much higher and hence this approximation is not applicable. In the present formulation, density has been considered variable in all the terms of the governing equations and hence full axisymmetric compressible flow equations have been solved. Other fluid properties, i.e. viscosity, thermal conductivity and specific heat are assumed to be functions of temperature.

The governing equations are rendered nondimensional using the radius of the tube and the fluid properties at 20°C as the reference quantities. Table 1 lists the nondimensional quantities. The nondimensional governing equations are given below.

Continuity equation:

$$\frac{\partial\tilde{\rho}}{\partial\tilde{t}}+\frac{1}{\tilde{r}}\frac{\partial\tilde{\rho}\tilde{r}\tilde{v}_r}{\partial\tilde{r}}+\frac{\partial\tilde{\rho}\tilde{v}_z}{\partial\tilde{z}}=0. \tag{1}$$

Radial momentum equation:

$$\frac{\partial\tilde{\rho}\tilde{v}_r}{\partial\tilde{t}}+\frac{1}{\tilde{r}}\frac{\partial\tilde{\rho}\tilde{r}\tilde{v}_r^2}{\partial\tilde{r}}+\frac{\partial\tilde{\rho}\tilde{v}_z\tilde{v}_r}{\partial\tilde{z}}=-\frac{\partial\tilde{p}_d}{\partial\tilde{r}}+\frac{4}{3}\frac{1}{\tilde{r}}\frac{\partial}{\partial\tilde{r}}\left(\tilde{r}\tilde{\mu}\frac{\partial\tilde{v}_r}{\partial\tilde{r}}\right)$$
$$-\frac{2}{3}\frac{1}{\tilde{r}}\frac{\partial}{\partial\tilde{r}}\left(\tilde{r}\tilde{\mu}\frac{\partial\tilde{v}_z}{\partial\tilde{z}}\right)-\frac{2}{3}\frac{1}{\tilde{r}}\frac{\partial(\tilde{\mu}\tilde{v}_r)}{\partial\tilde{r}}-\frac{4}{3}\frac{\tilde{\mu}}{\tilde{r}^2}\tilde{v}_r$$
$$+\frac{2}{3}\frac{\tilde{\mu}}{\tilde{r}}\frac{\partial\tilde{v}_r}{\partial\tilde{r}}+\frac{2}{3}\frac{\tilde{\mu}}{\tilde{r}}\frac{\partial\tilde{v}_z}{\partial\tilde{z}}+\frac{\partial}{\partial\tilde{z}}\left(\tilde{\mu}\frac{\partial\tilde{v}_z}{\partial\tilde{r}}\right)+\frac{\partial}{\partial\tilde{z}}\left(\tilde{\mu}\frac{\partial\tilde{v}_r}{\partial\tilde{z}}\right). \tag{2}$$

Axial momentum equation:

$$\frac{\partial\tilde{\rho}\tilde{v}_z}{\partial\tilde{t}}+\frac{1}{\tilde{r}}\frac{\partial\tilde{\rho}\tilde{r}\tilde{v}_r\tilde{v}_z}{\partial\tilde{r}}+\frac{\partial\tilde{\rho}\tilde{v}_z^2}{\partial\tilde{z}}=-\frac{\partial\tilde{p}_d}{\partial\tilde{z}}+Gr\,\tilde{\rho}\left(\frac{\theta-1}{\theta_{w1}-1}\right)$$
$$+\frac{1}{\tilde{r}}\frac{\partial}{\partial\tilde{r}}\left(\tilde{r}\tilde{\mu}\frac{\partial\tilde{v}_z}{\partial\tilde{r}}\right)+\frac{1}{\tilde{r}}\frac{\partial}{\partial\tilde{r}}\left(\tilde{r}\tilde{\mu}\frac{\partial\tilde{v}_r}{\partial\tilde{z}}\right)$$
$$+\frac{4}{3}\frac{\partial}{\partial\tilde{z}}\left(\tilde{\mu}\frac{\partial\tilde{v}_z}{\partial\tilde{z}}\right)-\frac{2}{3}\frac{\partial}{\partial\tilde{z}}\left(\tilde{\mu}\frac{1}{\tilde{r}}\frac{\partial\tilde{r}\tilde{v}_r}{\partial\tilde{r}}\right). \tag{3}$$

Energy equation:

$$\rho\tilde{C}_p\frac{\partial\theta}{\partial\tilde{t}}+\tilde{\rho}\tilde{C}_p\tilde{v}_r\frac{\partial\theta}{\partial\tilde{r}}+\tilde{\rho}\tilde{C}_p\tilde{v}_z\frac{\partial\theta}{\partial\tilde{z}}$$
$$=\frac{1}{Pr}\frac{1}{\tilde{r}}\frac{\partial}{\partial\tilde{r}}\left(\tilde{r}\tilde{k}\frac{\partial\theta}{\partial\tilde{r}}\right)+\frac{1}{Pr}\frac{\partial}{\partial\tilde{z}}\left(\tilde{k}\frac{\partial\theta}{\partial\tilde{z}}\right). \tag{4}$$

In Table 1, r_1 is the radius of the tube, r_2 is the outer radius of the diffuser, L is the height of the tube and s is the spacing between the diffuser discs. p is the static pressure at a point and p_a is the ambient pressure given by $p_0-\rho_0 gz$, where p_0 is the ambient pressure at the elevation of the inlet of the tube. T_{w1} and T_{w2} are the temperatures of the tube and the top disc respectively and T_0 is the ambient temperature. $\dot{m}$ is the mass flow rate of air through the system. q_{tube} and

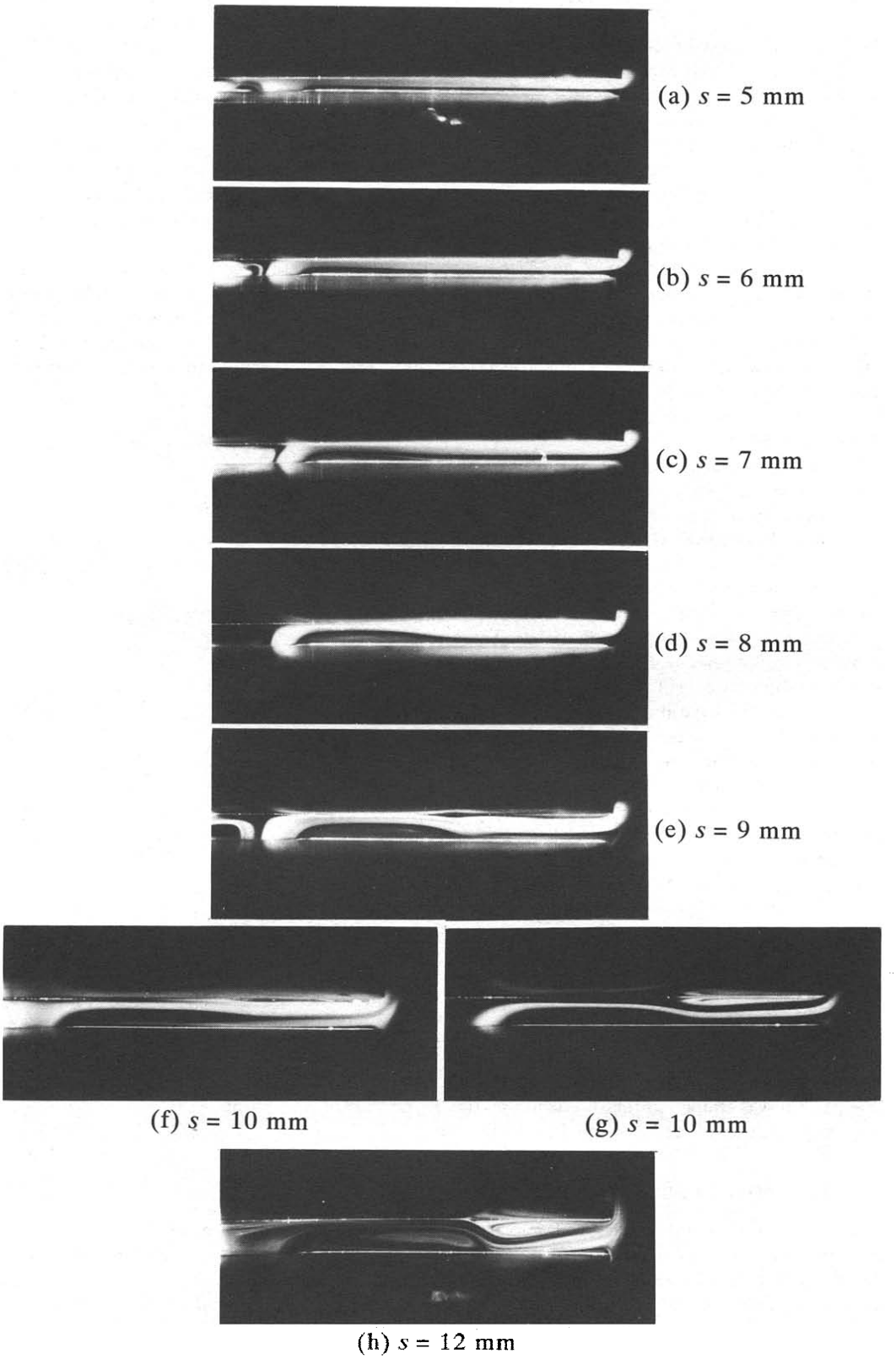

FIG. 3. Observed flow patterns in the diffuser for different diffuser spacings.

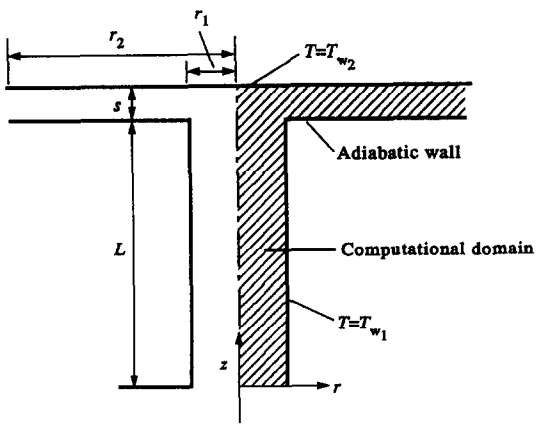

FIG. 4. Computational domain.

Table 1. Non-dimensional quantities

$\tilde{r}=\frac{r}{r_1}$	$\tilde{\rho}=\frac{\rho}{\rho_0}$	$\tilde{z}=\frac{z}{r_1}$
$\tilde{\mu}=\frac{\mu}{\mu_0}$	$\tilde{t}=\frac{tv_0}{r_1^2}$	$\tilde{k}=\frac{k}{k_0}$
$\tilde{v}_r=\frac{v_r r_1}{v_0}$	$\tilde{C}_p=\frac{C_p}{C_{p_0}}$	$\tilde{v}_z=\frac{v_z r_1}{v_0}$
$Pr=\frac{\mu_0 C_{p_0}}{k_0}$	$\tilde{p}_d=\frac{(p-p_a)r_1^2}{\rho_0 v_0^2}$	$A=\frac{L}{r_1}$
$\theta=\frac{T}{T_0}$	$\tilde{s}=\frac{s}{r_1}$	$\theta_{w1}=\frac{T_{w1}}{T_0}$
$\tilde{r}_2=\frac{r_2}{r_1}$	$\theta_{w2}=\frac{T_{w2}}{T_0}$	$Gr=\frac{gr_1^3(T_{w1}-T_0)}{T_0 v_0^2}$
$\tilde{m}=\frac{\dot{m}}{\rho_0 v_0 r_1}$	$Gr^*=\frac{Gr}{A}$	$\tilde{q}_{tube}=\frac{q_{tube}r_1}{k_0 T_0}$
$\tilde{Q}_{tube}=\frac{Q_{tube}}{k_0 T_0 r_1}$	$\tilde{q}_{disc}=\frac{q_{disc}r_1}{k_0 T_0}$	$\tilde{Q}_{disc}=\frac{Q_{disc}}{k_0 T_0 r_1}$

q_{disc} are the heat flux at the tube wall and the top disc respectively. Q_{tube} is the total heat input from the tube wall and Q_{disc}, the total heat transferred to the top disc. Subscript 0 refers to the properties of the fluid at the ambient temperature.

3.1. *Boundary Conditions*

Inlet to the tube. The effect of different inlet boundary conditions on natural convective flow through a vertical channel has been investigated in the literature. Pressure at the inlet is one of the most important boundary conditions. Most studies on natural convection through vertical ducts have assumed atmospheric pressure at the inlet. Aihara [12] showed that in the case of a parallel plate channel, neglecting the pressure drop due to acceleration of the surrounding fluid towards the inlet could affect the results significantly at high Rayleigh numbers. The same conclusion was reached by Dyer [8] and Fujii *et al.* [9] for a vertical tube. In the present study, the inlet pressure condition recommended by the above authors, namely, stagnation pressure at the inlet being equal to the ambient pressure at the same elevation, is used. Viscous losses during acceleration of the fluid from the ambient to the tube inlet have been neglected and thus, the static pressure and the velocity at the inlet are related by Bernoulli's equation.

The fluid is assumed to enter the tube axially, i.e. the radial velocity at the tube inlet is taken to be zero. It follows from the continuity equation that the normal gradient of axial velocity at this boundary is zero. The fluid at the inlet is assumed to be at ambient temperature. The boundary conditions at the inlet can be summarized as:

$$\tilde{p}_d=-\tfrac{1}{2}\tilde{\rho}\tilde{v}_z^2;\quad \tilde{v}_r=0;\quad \frac{\partial\tilde{\rho}\tilde{v}_z}{\partial\tilde{z}}=0;\quad \theta=1$$
$$\text{for } 0\leqslant\tilde{r}<1;\quad \tilde{z}=0.$$

Exit of the diffuser. The flow at the exit of the system can be considered as a jet entering a quiescent medium. This situation is different from the flow at the inlet where suction causes inflow of fluid from all directions and the resulting flow from the quiescent ambient to the inlet of the tube is like potential flow. Due to the nature of the inlet flow, the use of Bernoulli's equation for the pressure there is appropriate. However, at the exit, since the flow emerges like a jet, the boundary condition of the static pressure being equal to the local ambient is more appropriate. (Please see the discussion on the effect of outer radius of the diffuser on the flow and pressure variation inside the diffuser in Section 4.2.1.)

The flow at the exit is assumed to be radial. Thus the boundary conditions at the exit are:

$$\tilde{p}_d=0;\quad \frac{\partial\tilde{\rho}\tilde{r}\tilde{v}_r}{\partial\tilde{r}}=0;\quad \tilde{v}_z=0;\quad \frac{\partial\theta}{\partial\tilde{r}}=0$$
$$\text{for } \tilde{r}=\tilde{r}_2;\quad A<\tilde{z}<A+\tilde{s}.$$

Axis of the tube. Due to symmetry, the radial velocity and the radial gradients of the axial velocity and temperature are zero at this boundary.

$$\tilde{v}_r=0;\quad \frac{\partial\tilde{\rho}\tilde{v}_z}{\partial\tilde{r}}=0;\quad \frac{\partial\theta}{\partial\tilde{r}}=0$$
$$\text{for } \tilde{r}=0;\quad 0<\tilde{z}<A+\tilde{s}.$$

Solid walls. At all the fixed boundaries, the no-slip condition causes the velocities to be zero. The tube wall is maintained at a constant temperature T_{w1}. The top disc of the diffuser is at a lower temperature T_{w2}. The bottom disc of the diffuser is taken to be adiabatic. At all solid walls:

$$\tilde{v}_r = 0; \quad \tilde{v}_z = 0.$$

Tube wall: $\theta = \theta_{w1}$ for $\tilde{r} = 1.0; 0 \leqslant \tilde{z} \leqslant A$
Top disc: $\theta = \theta_{w2}$ for $0 \leqslant \tilde{r} \leqslant \tilde{r}_2; \tilde{z} = A + \tilde{s}$
Bottom disc: $\partial\theta/\partial\tilde{z} = 0$ for $1 \leqslant \tilde{r} \leqslant \tilde{r}_2; \tilde{z} = A.$

3.2. *Equations For Property Variation*

The ideal gas law is used for determining the density at each control volume from the temperature field. The effect of pressure variation on density has been neglected in the buoyancy term. The contribution of the pressure term on the density variation is almost five orders of magnitude less than that of the temperature term. For viscosity and thermal conductivity variation, Sutherland's law [13] has been used. For specific heat, cubic polynomials fitted to the available data [14] in the temperature range of 250–1800 K have been used. These expressions are listed below.

$$\tilde{k} = \theta^{3/2}\left[\frac{1+\tilde{S}_k}{\theta+\tilde{S}_k}\right] \quad \text{where } \tilde{S}_k = \frac{194.44}{T_0}$$

$$\tilde{\mu} = \theta^{3/2}\left[\frac{1+\tilde{S}_\mu}{\theta+\tilde{S}_\mu}\right] \quad \text{where } \tilde{S}_\mu = \frac{110.56}{T_0}$$

$$\tilde{C}_p = -0.1291\tilde{T}^3 + 0.3408\tilde{T}^2 - 0.0691\tilde{T} + 0.9987$$

where $\tilde{T} = T/1000$, T being the absolute temperature.

The governing equations have been solved using the finite difference algorithm SIMPLER [15]. The computational domain is divided into control volumes over which the governing equations are integrated to obtain algebraic expressions for the values of the flow variables in these control volumes. The hybrid scheme, which is a combination of central differencing and upwinding, has been used for discretization of the advection terms. A non-uniform grid has been used both in the r and z directions. The ratio of minimum to maximum grid size, in both the radial and axial directions is about 10^{-2}. The number of grid points in the r and z directions have been chosen as demanded by the aspect ratio and the outer radius of the diffuser. Typically, for an aspect ratio of 15, 20×50 grid points have been used in the tube while in the diffuser, the grid used varies between 40×18 and 65×18 as $\tilde{r}_2$ varies from 2 to 8. The grid has been so clustered as to have a fine mesh in the neighbourhood of the bend.

The equations are solved by marching in time till a steady state solution is obtained. In the steady state, the transient term in the governing equation should be equal to zero. In the numerical solution, the magnitude of this term as compared to the other terms in the equation should become small at steady state. In the present study, when the r.m.s. value of the ratio of unsteady term to the highest term in the governing equation is less than 10^{-4}, the solution is assumed to have attained steady state.

The solutions were checked for grid independence for a typical case by doubling the number of grid points in both the r and z directions. It was found that the mass flow rates and the heat fluxes in the two cases were not different by more than 2%. The flow pattern did not vary with the mesh size. The code was also validated for the open tube case with the results of Kageyama and Izumi [6]. The results were found to be in agreement within 5%.

4. RESULTS AND DISCUSSION

The geometrical and thermal parameters which affect the flow include the radius r_1 and height L of the tube, outer radius of the diffuser r_2, the spacing between the diffuser discs s and the temperature of the tube wall T_{w1} and the top disc T_{w2}. These dimensional quantities could be grouped in order to define the non-dimensional parameters which govern the flow, namely the Grashof number Gr, aspect ratio A, spacing $\tilde{s}$, radius ratio $\tilde{r}_2$ and temperatures θ_{w1} and θ_{w2}, defined in Table 1. The effect of Gr and A can be combined into a single parameter Gr^*. All earlier investigations on natural convection flow through vertical channels have considered Gr^* as the main parameter. In the present study also, results have been presented for different values of Gr^*.

4.1. *Simulation Of Experimental Cases*

In order to validate the computer program, a simulation of the cases photographed in flow visualization experiments has been carried out. The tube wall temperatures measured in the experiments have been fitted to a second order polynomial to provide the boundary condition for the simulation. The wall temperature profile is shown in Fig. 2(c). The temperature of the top disc used in the simulation was also obtained from the experiment. For the simulation, the Grashof number has been computed based on the mean tube wall temperature of 695 K. The top disc temperature was 397 K. The value of Gr^* for these cases is 3×10^4 and $\tilde{r}_2$ is 5.875, while $\tilde{s}$ varies from 0.25 to 0.5.

The flow visualization showed that the flow pattern in the diffuser changes considerably with spacing of the diffuser (Figs. 3(a)–(f)). At all spacings, the flow separates at the bend of the tube forming a separation bubble at the entrance of the diffuser. At lower spacings, this separation bubble is small in size, and grows with increase in spacing.

The simulation results also show very similar patterns. Figure 5(a) presents the streamlines for the spacing of 5 mm ($\tilde{s} = 0.25$). The flow is found to bend with a small separation bubble in this case, whereas at higher spacing of 10 mm ($\tilde{s} = 0.5$), the separation bubble is much larger (Fig. 5(f)). We can see that the flow patterns in the corresponding cases presented in Figs. 5(a)–(f) agree very well with those presented in Figs. 3(a)–(f). However, no attempts have been made in the present work to simulate the unsteadiness observed in the flow at higher spacings. (In Fig. 5, the diffuser region has been enlarged in the z direction by a factor of about three for greater clarity.)

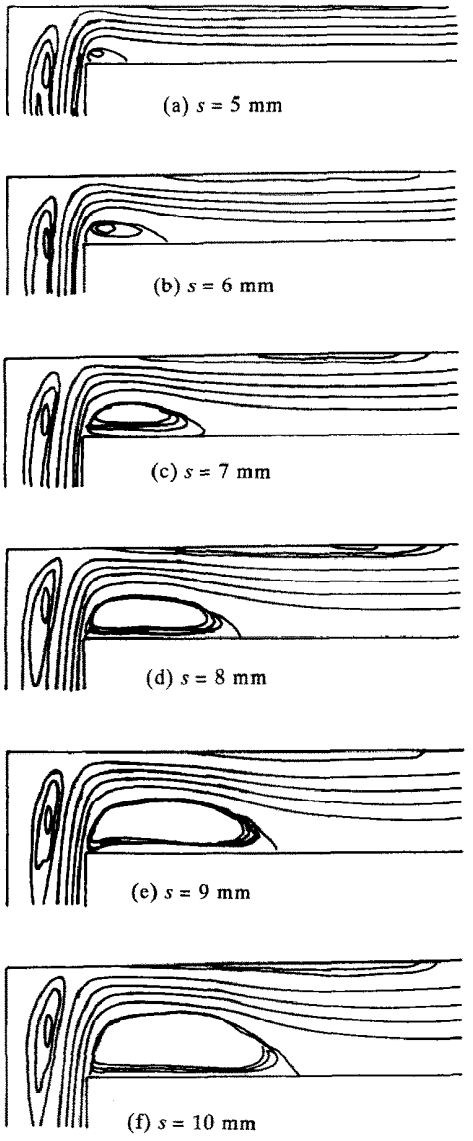

FIG. 5. Streamline patterns in the diffuser obtained from simulation of experimental cases.

4.2. *Simulation Of Constant Wall Temperature Case*

Further simulations were carried out using a constant tube wall temperature to study the effect of the various parameters on the flow field. In the present study, the effect of three parameters, Gr^*, $\tilde{s}$ and $\tilde{r}_2$ on the flow field and heat transfer is investigated. θ_{w1} and θ_{w2} have been maintained constant at 3.32 and 1.27 respectively corresponding to the dimensional temperatures of 700°C at the tube wall and 100°C at the top disc.

The case corresponding to $Gr^* = 5 \times 10^4$, $\tilde{s} = 0.5$ and $\tilde{r}_2 = 2.0$ forms the base line case of this study. $\tilde{s}$ has been varied from 0.1 to 0.5 keeping Gr^* and $\tilde{r}_2$ at their baseline values to study the effect of spacing. Likewise, $\tilde{r}_2$ has been varied from 2.0 to 8.0 keeping Gr^* and $\tilde{s}$ at their baseline values to study the effect of the outer radius of the diffuser; Gr^* values of 6×10^3 and 9×10^2 have been investigated with $\tilde{s}$ and $\tilde{r}_2$ at their baseline values to predict the effect of Gr^*.

The simulation results indicate a strong variation of the local as well as the global quantities with the above three parameters. The local quantities include the temperature, pressure and velocity fields and the heat fluxes at the tube wall and the top disc of the diffuser. The global quantities are the mass flow rate, total heat input from the tube wall and the total heat transferred to the top disc of the diffuser.

4.2.1. *Local quantities*

Flow pattern. The streamline pattern for the baseline case ($Gr^* = 5 \times 10^4$, $\tilde{s} = 0.5$, $\tilde{r}_2 = 2.0$) is plotted in Fig. 6(a). It can be seen that the flow separates at the bend and hugs the top disc until it leaves the diffuser, unlike those shown in Figs. 5(a)–(f) where the flow reattaches itself to the bottom surface of the diffuser. Figures 6(b) and (c) show the effect of $\tilde{s}$ on the flow pattern. At $\tilde{s} = 0.25$, there is a very small separation bubble seen, as the flow separates and reattaches (Fig. 6(b)). At $\tilde{s} = 0.1$ (Fig. 6(c)), no separation is observed, and the flow remains attached to both diffuser walls throughout.

The separation of the flow is due to the centrifugal forces coming into play when the flow negotiates the bend. There are two reasons for the flow remaining almost unseparated for small spacings. Firstly at small

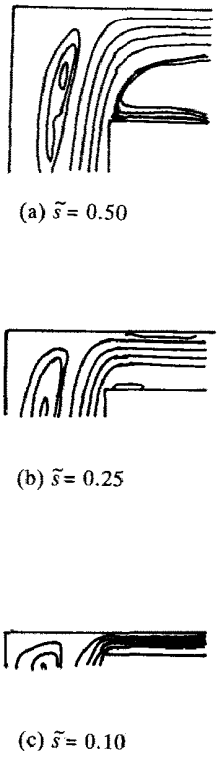

FIG. 6. Effect of spacing on the flow patterns in the diffuser ($Gr^* = 5 \times 10^4$, $\tilde{r}_2 = 2.0$).

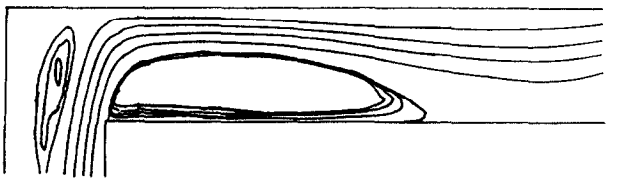

(a) $\tilde{r}_2 = 6.0$

(b) $\tilde{r}_2 = 8.0$

FIG. 7. Effect of outer radius on the flow pattern in the diffuser ($Gr^* = 5 \times 10^4$, $\tilde{s} = 0.5$).

spacings, the mass flow rate and hence the velocities are lower. A low velocity flow can traverse a sharp bend more easily without separation than a high velocity flow due to lower centrifugal forces. Secondly, due to the presence of the top disc close to the bottom disc at lower spacings, the flow is forced to remain attached to both the walls. When the spacing is large, due to high velocities and larger clearance, the flow tends to be closer to the top wall resulting in separation of the flow at the bend. (In all these figures, the diffuser region is enlarged in the z direction by a factor of two.)

After the separation at the bend, the velocities decrease due to deceleration of the flow in the diffuser. If the diffuser is long enough, the flow can be expected to spread again and reattach itself to the bottom wall (Fig. 6(b)). This can also be seen in Figs. 7(a) and (b), which correspond to $\tilde{r}_2$ values of 6.0 and 8.0 respectively, with Gr^* and $\tilde{s}$ kept at their baseline value. In Fig. 6(a), where $\tilde{r}_2 = 2.0$, the diffuser length is not sufficient for reattachment. In the cases where reattachment takes place, the size of the separation bubble is found to be independent of the outer radius of the diffuser. In both Figs. 7(a) and (b), the reattachment lengths are found to be the same. This is because the mass flow rate and the velocity at the bend are not affected significantly by the increase in the outer radius of the diffuser, particularly at large spacings. Thus the effect of centrifugal forces at the bend remains the same, resulting in little change in reattachment lengths.

Since the separation of the flow at the bend depends on the velocity of the flow at the tube exit, at lower Gr^*, the flow will be less prone to separation. The stream lines in the diffuser region for $Gr^* = 6 \times 10^3$ and $Gr^* = 9 \times 10^2$ are plotted in Figs. 8(a) and (b), respectively. A comparison of Figs. 6(a), 8(a) and 8(b) shows clearly how the flow depends on Gr^*. The flow goes without reattaching at high Gr^* (Fig. 6(a)), while at a lower Gr^*, the flow reattaches (Fig. 8(a)), or goes without separating (Fig. 8(b)).

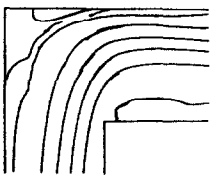

(a) $Gr^* = 6 \times 10^3$

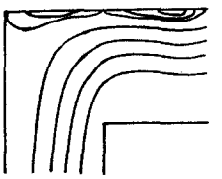

(b) $Gr^* = 9 \times 10^2$

FIG. 8. Effect of Gr^* on the flow patterns in the diffuser ($\tilde{s} = 0.5$, $\tilde{r}_2 = 2.0$).

It is interesting to note that the reattachment length is a function of both $\tilde{s}$ and Gr^*. This can be seen from Figs. 6(a), (b), 7(a), (b) and 8(a), (b). The reattachment length in Fig. 6(b) which corresponds to $\tilde{s} = 0.25$ is quite small compared to that seen in Figs. 7(a) and (b), which corresponds to $\tilde{s} = 0.5$. Similarly, the flow passes without reattaching in Fig. 6(a), which corresponds to $Gr^* = 5 \times 10^4$, while in Fig. 8(a), which corresponds to a lower Gr^* of 6×10^3, the flow is almost attached for the same $\tilde{s}$ and $\tilde{r}_2$. Figure 8(b) shows the case of $Gr^* = 9 \times 10^2$, where the flow does not separate at all. These observations can be explained by the fact that the bubble length is higher for a larger flow rate. As Gr^* or $\tilde{s}$ is increased, the flow rate increases and hence the length of reattachment is higher.

The behaviour of the flow with varying spacing is very similar to that suggested by Moller [16] for forced flow through a similar configuration, but Moller did not present any experimental or computational data in support of his comment. Saad *et al.* [17] have carried out the numerical simulation of forced flow and heat transfer for an axisymmetric jet impinging on a plate along with another confining plate, a configuration similar to that of present study. For a mass flow rate comparable to that of the baseline case of the present work, and for $\tilde{s} = 2.0$ and $\tilde{r}_2 = 4.0$, the flow pattern obtained by them is qualitatively very similar to that obtained in the baseline case of present study ($\tilde{s} = 0.5$ and $\tilde{r}_2 = 2.0$). The flow hugs the impingement plate throughout its length with the formation of a recirculation zone in most of the region between the plates. The flow does not reattach to the confining plate. However, for a smaller Re and smaller spacing between the plates, they found the flow to be reattached to the confining plate.

This suggests that in the present case, even though the flow is driven by natural convection in the system as a whole, the flow at the bend and in the diffuser region behaves similar to a forced convection problem. The size of the recirculation zone is affected in the buoyancy driven flow by $\tilde{s}$ and Re similar to forced convection flows.

At different values of Gr^*, the streamline pattern in the central region of the tube and the stagnation zone is also different (Figs. 6(a) and 8(b)). For $Gr^* = 5 \times 10^4$ (Fig. 6(a)), the region near the central axis has a recirculation zone, which extends almost up to the entrance of the tube (not shown here). However, at lower Gr^*, the stagnation or the recirculation zone is confined only to a small region near the top disc (Fig. 8(b)). There is no occurrence of the central recirculation zone, and the main stream of the flow occupies the whole cross section of the tube. At high Gr^*, the buoyancy forces are predominant over diffusion, causing the larger velocity flow to be confined to a region close to the tube wall, where the buoyancy effects are high. At high Gr^*, since diffusion of both heat and momentum is low, the fluid in the core of the tube remains at a lower temperature and does not acquire higher velocities. At $Gr^* = 9 \times 10^2$, diffusion effects are much stronger and so, the velocities as well as the temperatures near the central axis are higher. The recirculation zone for higher velocities is due to the impingement of high velocity fluid on the top disc.

Thus the flow pattern in the stagnation region is a strong function of the velocity profile of the impinging jet. The central recirculation zone is predominant when the peak velocity of the impinging jet is away from the axis of symmetry, as in the case of high Gr^*. When the velocity peak lies on the central axis as in the case of a forced jet, no recirculation is seen in the stagnation region.

Velocity field

Axial velocity profiles in the tube. Figure 9(a) shows the comparison of velocity profiles at the exit of the tube for $\tilde{s} = 0.1$ and 0.5 ($Gr^* = 5 \times 10^4$, $\tilde{r}_2 = 2.0$) with that for an open tube. For smaller spacings, the velocity shows a peak closer to the tube wall and rapidly drops down to almost zero near the centre. Due to high resistance from the top wall, fluid in most parts of the tube is not able to acquire high velocities. When the spacing is increased, the effect of the top wall on the profile at the exit of the tube decreases. Thus the shape of the profile for $\tilde{s} = 0.5$ is closer to that for the open tube. In the case of the open tube, the velocities in the central core are small but still positive, while for $\tilde{s} = 0.5$, impingement of the jet on the top wall results in a recirculation near the central axis and hence the velocities there are negative. For $\tilde{s} = 0.1$, the impingement velocities are too small to cause any strong recirculation.

Effect of Gr^* on variation of axial velocity profile at the exit of the tube is shown in Fig. 9(b). When the Grashof number is high, the buoyancy force dominates and hence the velocity peak is close to the wall of the tube. When the Grashof number is low, the diffusion of heat and momentum is dominant and hence, the maximum velocity shifts to the centre of the tube. The velocity profile, in this case is almost flat.

Radial velocity profiles in the diffuser. The behaviour of the flow in the diffuser as shown in the streamline patterns, can also be seen in the velocity profiles. Figure 10 shows the radial velocity profiles in the diffuser for different values of $\tilde{s}$ at $Gr^* = 5 \times 10^4$ and $\tilde{r}_2 = 2.0$. At the entrance to the diffuser, the profile is similar in shape for all the spacings and is almost symmetric about the middle plane of the diffuser. For $\tilde{s} = 0.1$ (Fig. 10(a)), the flow has a parabolic profile throughout the diffuser. When the spacing is increased ($\tilde{s} = 0.25$), there is an asymmetry in the velocity profile in the region away from the entrance (Fig. 10(b)). Here, the velocities closer to the bottom wall have small negative values due to separation at the bend. After reattachment to the bottom wall, the flow tends to attain a more symmetric and parabolic shape. For $\tilde{s} = 0.5$, the asymmetry in the profile is more pronounced. The separation bubble is much bigger, the

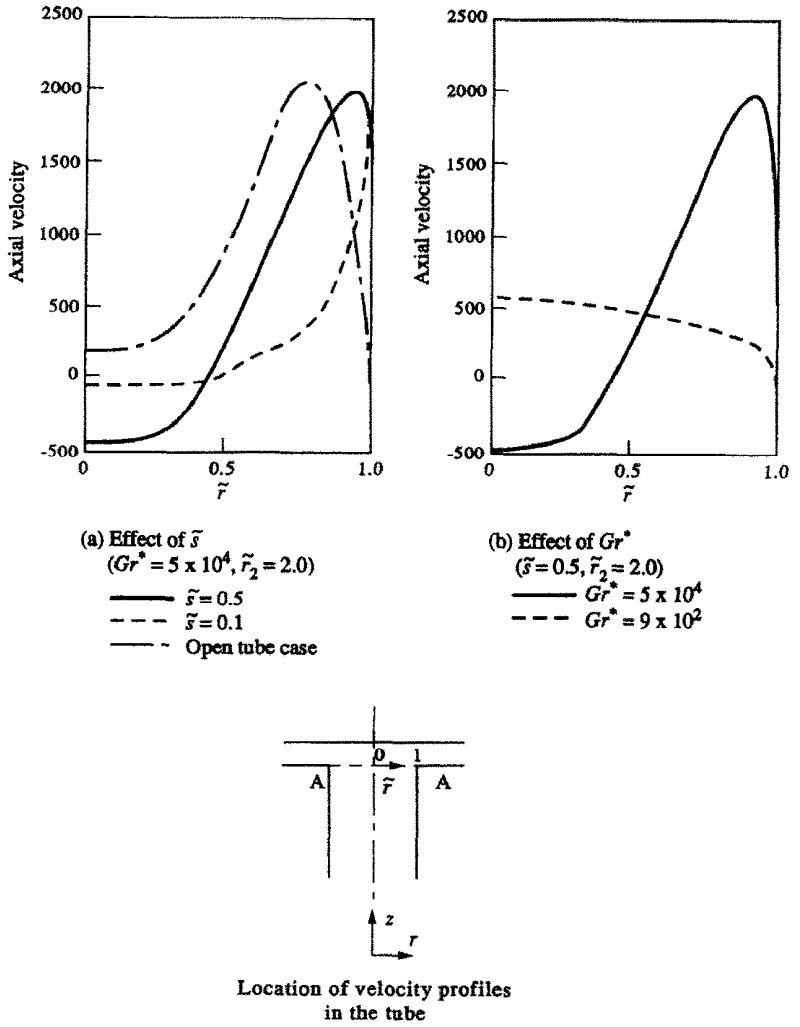

FIG. 9. Axial velocity profiles at tube exit.

negative velocities near the bottom wall are higher in magnitude and prevail for a greater length (Fig. 10(c)).

Pressure. In the present flow configuration, pressure is an important parameter, due to the combination of three different flow regimes—the tube flow, stagnation point flow and the diffuser flow. Particularly in the diffuser, the pressure profiles show interesting trends due to the interaction of viscous effects and the deceleration in the diffuser.

Figure 11(a) shows the variation in pressure defect in the stagnation zone and the diffuser region for $Gr^* = 5 \times 10^4$, $\tilde{r}_2 = 2.0$ and three different values of $\tilde{s}$. It has been found that for a small spacing ($\tilde{s} = 0.1$), pressure in the diffuser decreases monotonically showing that in this case pressure drop due to viscous effects is higher than the pressure increase due to the deceleration in the diffuser. As the spacing is increased ($\tilde{s} = 0.25$), the deceleration in the diffuser predominates over viscous effects. This induces an adverse pressure gradient in the diffuser. Since the pressure at the exit of the diffuser is ambient, this adverse pressure gradient causes the pressure inside the diffuser to be below atmospheric. Further increase in spacing ($\tilde{s} = 0.5$) causes the pressure to be more uniform indicating a decrease in the effect of the diffuser.

The effect of outer radius on the diffuser pressure is insignificant at smaller spacings, while at higher spacings, an increase in the outer radius has a more significant effect on the pressure variation. For $\tilde{r}_2 = 2.0$ and at $\tilde{s} = 0.25$, pressure is found to increase monotonically in the diffuser up to the exit (Fig. 11(a)). As the outer radius is increased, the increase in pressure continues only up to $\tilde{r} \approx 2$, after which it decreases slowly (Fig. 11(b)). This suggests that the effect of deceleration is predominant only up to $\tilde{r} \approx 2$. Beyond this point, the pressure drop due to viscous effects and the pressure increase due to deceleration seem to almost balance each other.

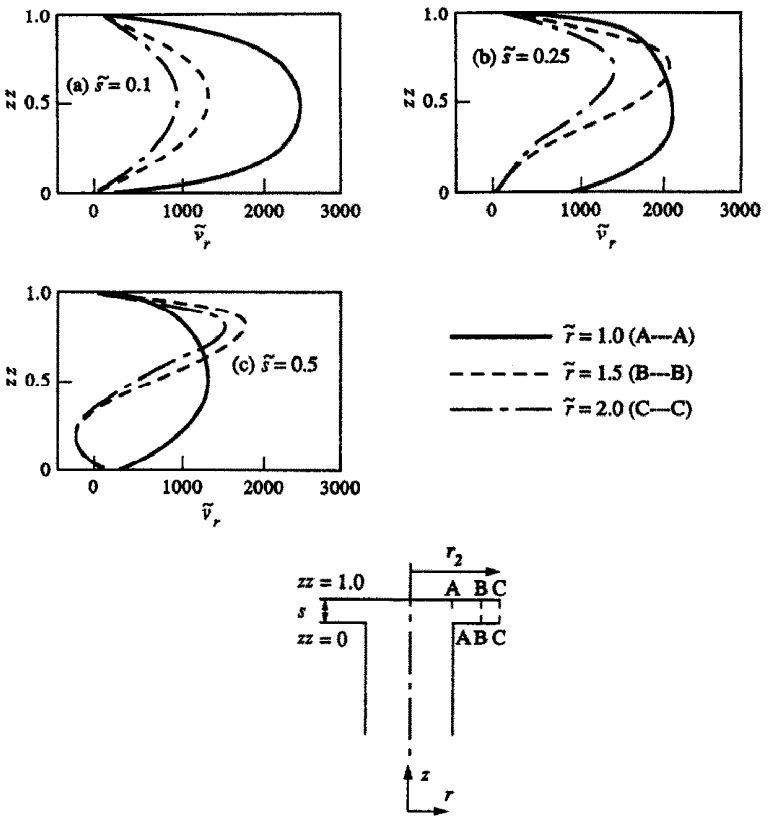

FIG. 10. Radial velocity profiles in diffuser ($Gr^* = 5 \times 10^4$, $\tilde{r}_2 = 2.0$).

A comparison of pressure variation with flow patterns shows that when there is no separation, pressure is monotonically decreasing in the diffuser (Figs. 11(a), (b)). For $\tilde{s} = 0.25$, there is an adverse pressure gradient up to $\tilde{r} \approx 2$, but the separation bubble is found to be small and confined to the region close to the entrance (Fig. 6(b)). For $\tilde{s} = 0.5$, the separation bubble is much bigger and extends up to $\tilde{r} \approx 4$. In the separation zone as the flow is confined to a small region away from the wall, it can be considered equivalent to reducing the effective spacing between the diffuser walls without increasing the viscous forces. This makes the effect of deceleration predominant and hence the adverse pressure gradient in the region of separation. After reattachment, the pressure rise due to deceleration and the pressure drop due to viscous effects tend to balance each other.

It may be noted that the variation in the absolute value of pressure through the diffuser under any of the above conditions is marginal in comparison with the pressure drop across the bend. While the absolute value of pressure can drop by 30 Pa at the bend, in the diffuser region, the variation is not more than 2.0 Pa. It has already been seen that the extension of the outer radius of the diffuser beyond the reattachment zone does not affect the flow. Since the variation in the pressure in the diffuser is quite small, the boundary effects do not influence the inner details of the flow and heat transfer.

Temperature field

Temperature profiles at the tube exit. Figure 12(a) shows the effect of diffuser spacing on the temperature profiles at the tube exit. At $\tilde{s} = 0.1$, the fluid velocities are lower and are also confined to a smaller region near the tube wall, as compared to the case for $\tilde{s} = 0.5$. At smaller fluid velocities, the effect of diffusion is higher, resulting in higher fluid temperatures as seen in Fig. 12(a). At $\tilde{s} = 0.5$, stronger convection effects prevent the penetration of the effect of the wall temperature towards the central region of the tube, and hence the temperature in the centre of the tube is much lower.

Figure 12(b) shows the effect of Gr^* on the temperature profiles at the exit of the tube. As already explained in the last section for a given wall temperature, at lower Gr^* diffusion is stronger and the velocities are lower, causing the fluid temperatures to be higher.

Temperature profiles in the diffuser. Figure 13(a)

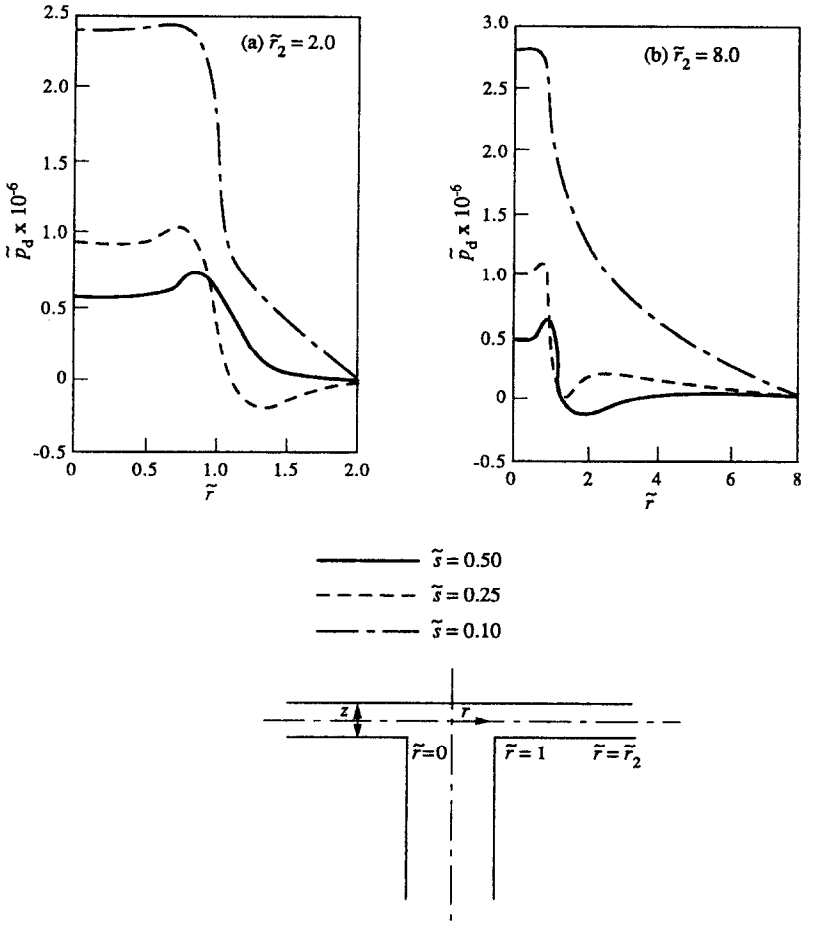

FIG. 11. Effect of spacing on pressure defect in the diffuser ($Gr^* = 5 \times 10^4$).

shows the temperature profiles in the diffuser for $Gr^* = 5 \times 10^4$, $\tilde{r}_2 = 2.0$ and different values of $\tilde{s}$. For $\tilde{s} = 0.1$, when there is no separation, the peak of the temperature profile lies on the adiabatic bottom disc, at all cross sections in the diffuser. Even at $\tilde{s} = 0.25$, where there is a small separation bubble, the temperature peak is still at the bottom disc (Fig. 13(b)). When $\tilde{s} = 0.5$ (Fig. 13(c)), and the separation is prominent, the peak of the temperature shifts away from the bottom disc and is very close to the peak of the radial velocity profile. The hot jet coming from the tube follows a trajectory closer to the top disc and because of the recirculation in the separation zone, the colder fluid from downstream is brought in towards the diffuser entrance causing the fluid temperature near the bottom disc to be lower.

Figure 13 also shows that the peak fluid temperature is lower for higher $\tilde{s}$. This is due to the lower bulk temperature of the fluid at the exit of the tube and hence at the entrance of the diffuser. For $\tilde{s} = 0.1$, temperatures decrease rapidly along the flow. At higher spacings, the fluid temperature falls less rapidly.

Heat flux to the top disc

Heat flux is a function of the temperature gradient at the wall. Since the top disc is maintained at constant temperature, the temperature gradient at this wall is determined only by the temperature of the fluid in its vicinity. In the present configuration, heat is being transferred to the top disc. So, the higher the fluid temperature at a point, the higher will be the heat flux at that point. The variation of the heat flux along the radius of the top disc is plotted in Fig. 14. Figure 14(a) shows the heat flux profile for $Gr^* = 5 \times 10^4$ and $\tilde{r}_2 = 2.0$ for different spacings. As already discussed, at lower spacing ($\tilde{s} = 0.1$), the temperature of the fluid at the tube exit is higher than that for larger spacings. This results in higher heat flux for $\tilde{s} = 0.1$. Since the temperature of the fluid at the tube exit is a maximum close to the tube wall, the heat flux to the top disc is also a maximum in the region above the tube wall. Towards the centre of the tube, where fluid temperatures are low, heat flux to the top disc is also lower. This result is quite different from the case of impingement of a forced jet [17] where the heat transfer is highest at the axis of symmetry.

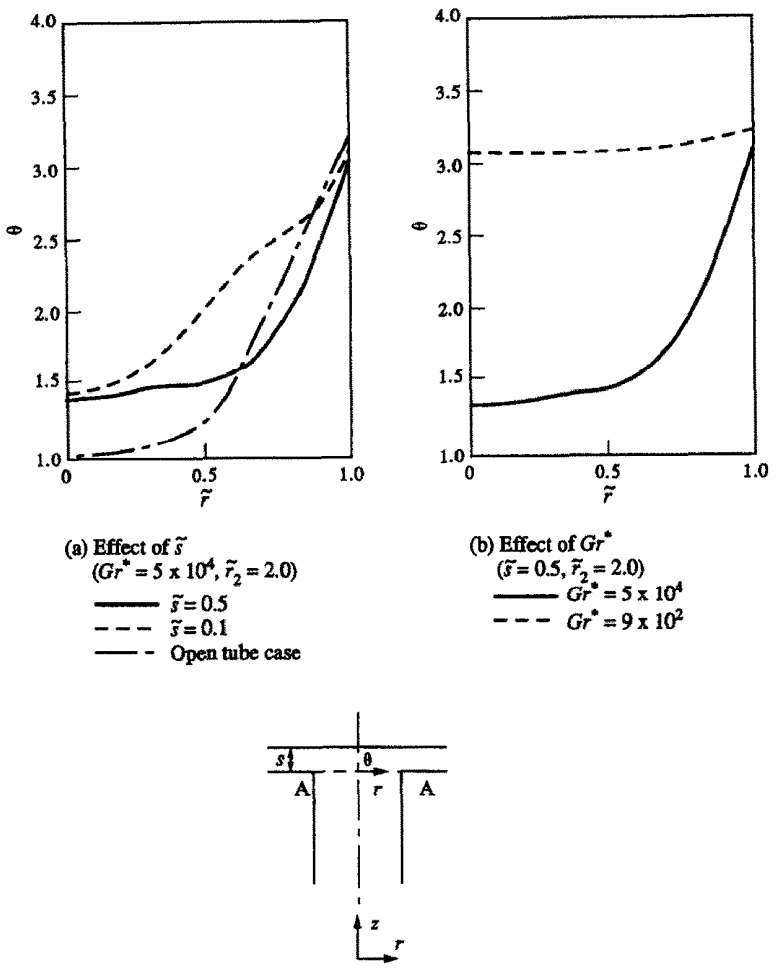

FIG. 12. Temperature profiles at tube exit.

The rise in heat flux from the centre of the tube to the diffuser entrance is much steeper for $\tilde{s} = 0.1$ than for higher spacings. It may be recollected that for $\tilde{s} = 0.1$, the temperature profile at the tube exit was found to be more uniform near the tube wall than for the higher spacing case (Fig. 12(a)). This should result in a more uniform heat flux in the stagnation zone for lower spacings. However, what is observed is just the opposite, i.e. for higher spacings ($\tilde{s} = 0.25$ and 0.5), the increase in heat flux from the centre of the disc to the diffuser entrance is more gradual. This can be explained by the fact that higher impingement velocities for larger spacings result in better mixing in the stagnation zone. Consequently, the temperatures of the fluid in the vicinity of the top disc are more uniform, causing more uniform fluxes in that region.

For $\tilde{s} = 0.1$, the heat flux to the top disc falls steeply in the diffuser region. This is because of the rapid fall in bulk temperature of the fluid which in turn is due to the higher rate of heat transfer near the entrance of the diffuser (Fig. 14(a)). For $\tilde{s} = 0.5$, the separation bubble at the entrance of the diffuser covers as much as half the diffuser spacing, as discussed earlier (Fig. 7(a)). Thus the effective spacing of the flow in this case is almost the same as that for the $\tilde{s} = 0.25$ case, which causes the heat flux curves for $\tilde{s} = 0.5$ and $\tilde{s} = 0.25$ to be very similar.

Since the increase in $\tilde{r}_2$ does not affect the flow pattern and the velocities significantly, the heat flux curves are not expected to change much with increase in $\tilde{r}_2$. This is confirmed by Fig. 14(b). It can be seen that the heat flux curves for higher $\tilde{r}_2$ are essentially an extension of the curve for lower $\tilde{r}_2$.

Figure 14(c) shows the effect of Gr^* on the heat flux to the top wall. At lower Gr^*, higher diffusion causes the temperatures to be high even in the centre of the tube. The impingement velocities are also high near the centreline. This results in the central region of the top disc having the maximum heat flux. On the other hand, for $Gr^* = 5 \times 10^4$, where both the fluid tem-

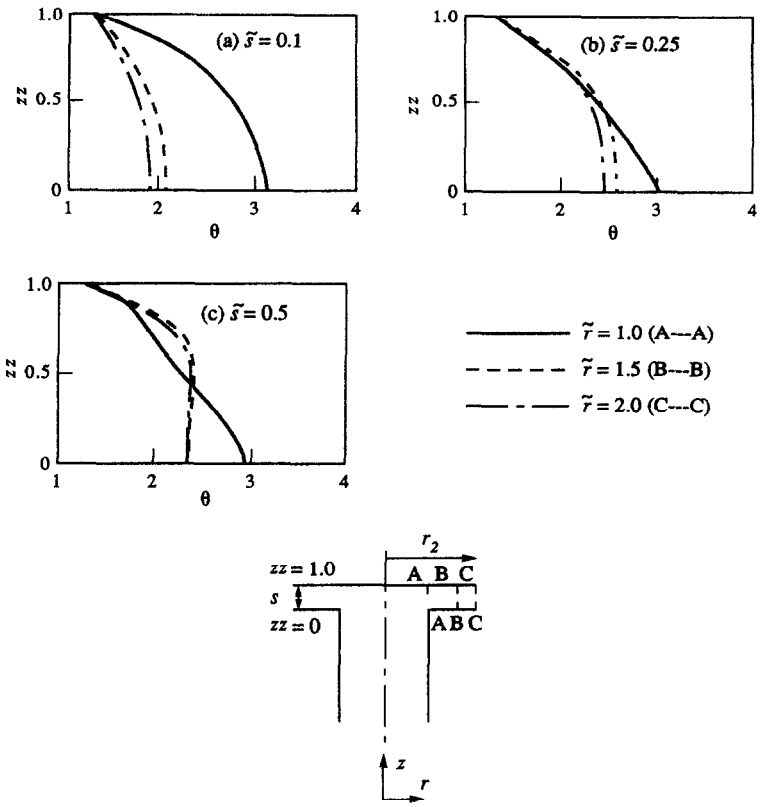

FIG. 13. Temperature profiles in the diffuser.

perature and the velocities are low in the central zone, heat fluxes are minimum in that region. In the diffuser, heat flux for $Gr^* = 9 \times 10^2$ is higher than that for $Gr^* = 6 \times 10^3$ due to higher fluid temperature in the former case. But the fluxes are a little lower than those for $Gr^* = 5 \times 10^4$. These are attributable to the fact that the heat flux depends on the bulk fluid temperature as well as the heat transfer coefficient, whose variations are non-uniformly dependent on the different parameters. Thus the net effect of a parameter on heat flux will depend on the combination of the effect on heat transfer coefficient and fluid temperature.

4.2.2. *Global quantities*

Mass flow rate. It is a characteristic feature of buoyancy-induced flow that the mass flow rate through the system is not known a priori and is determined by the interaction between the heat transfer and the fluid flow phenomena. Since the effectiveness of the heat transfer from the tube wall to the fluid and from the fluid to the top disc depend on the fluid velocities, the mass flow rate through the system is an important parameter in the present study.

In a buoyancy-induced flow, the mass flow is determined by the buoyancy forces and the resistance of the system to the flow. The fluid velocities are, in turn, dependent on the mass flow rate through the system. The buoyancy forces are governed by the tube wall temperature and the height of the tube. The radius of the tube, spacing between the diffuser discs and their outer radius determine the total resistance of the system. The higher the buoyancy forces, the higher should be the mass flow induced by it, whereas a greater resistance in the system will decrease the flow rate. The parameter Gr^* is representative of the magnitude of the buoyancy forces. $\tilde{s}$ and $\tilde{r}_2$, the non-dimensional spacing and the outer radius of the diffuser, determine the resistance of the system to the fluid flow. In Fig. 15(a), the non-dimensional mass flow rate $\tilde{m}$ has been further scaled with Gr for ease of representation.

At smaller spacing, the viscous loss in the diffuser is more and hence the mass flow rate is low. As the spacing is increased, the resistance of the system decreases and the flow rate increases. At large spacings, when the viscous effects are already low, a further increase in spacing causes very little increase in the mass flow. At very large spacings, the mass flow rate is expected to reach an asymptotic value close to that for the open tube case for a given Gr^*. It is found that this asymptotic value of $\tilde{m}$ is approached very slowly. Even at $\tilde{s} = 1.0$, the mass flow rate is found to

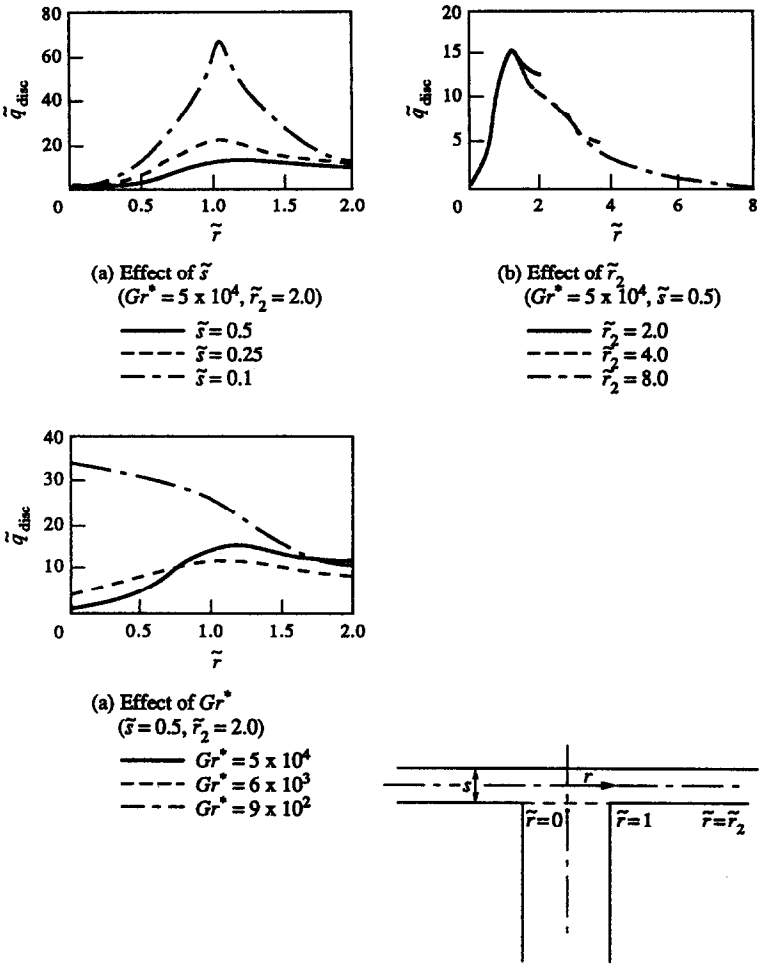

FIG. 14. Heat flux to the top disc.

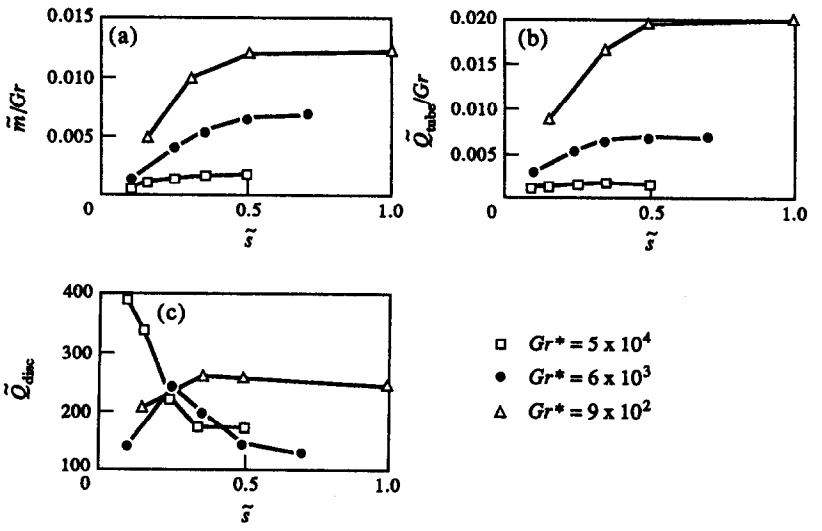

FIG. 15. Variation of global quantities with $\tilde{s}$.

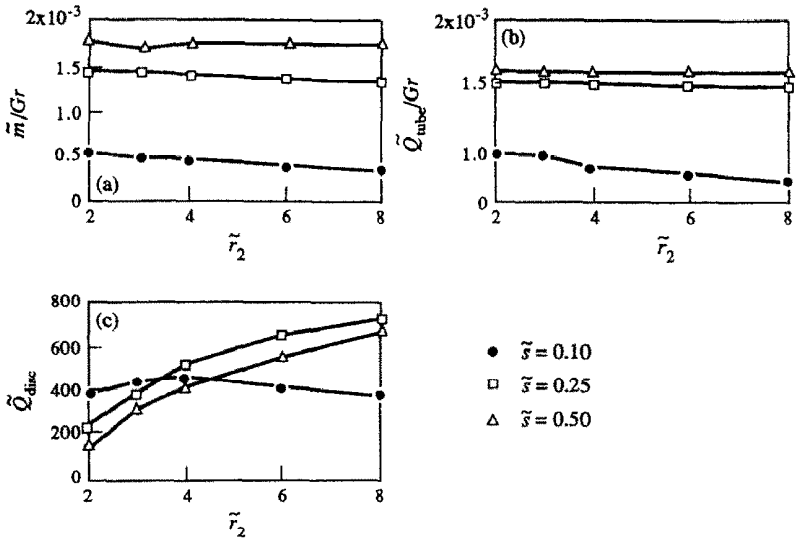

FIG. 16. Variation of global quantities with $\tilde{r}_2$.

be 20% lower than that of the open tube case. This is due to the fact that in an open tube the pressure is atmospheric at the exit of the tube. In the present configuration, even at the largest spacing considered, the pressure at the exit of the tube is higher than the ambient because of the presence of the top disc and the diffuser. Due to this effect, the mass flow through the system cannot be the same as that for an open tube. For the effect of the top disc and the diffuser to completely vanish, the pressure at the exit of the tube should be close to the ambient, for which the diffuser spacing needs to be much higher.

As can be seen in Fig. 16(a), the effect of the outer radius on the mass flow rate is very weak. At smaller spacings, an increase in $\tilde{r}_2$ causes a little reduction in $\tilde{m}$. This is expected since at small spacings, the increase in the outer radius of the diffuser adds to the already predominant viscous losses. At higher spacings, where the viscous losses are low, the increase in outer radius does not affect the flow significantly.

Total heat transfer from the tube

As has been discussed earlier, the heat flux from the tube to the fluid is a function of both the temperature of the fluid and the fluid velocities which determine the heat transfer coefficient. Since the fluid entering the tube is at ambient temperature, and the tube is maintained at a constant temperature, the total heat transfer to the fluid from the tube wall $\tilde{Q}_{tube}$ is essentially dependent on the fluid velocities. The higher the fluid velocities, the higher should be the total heat transfer to the fluid due to higher heat transfer coefficient. This can be seen in Figs. 15(b) and 16(b). The fluid velocities can be related directly to the mass flow rate. Thus, the curves for $\tilde{Q}_{tube}/Gr$ are very similar to the $\tilde{m}/Gr$ curves. The effect of an increase in the spacing is to increase $\tilde{Q}_{tube}$ rapidly first (Fig. 15(b)). But with further increase in spacing, $\tilde{Q}_{tube}$ increases more slowly, causing a plateau in the curve, as was the case with $\tilde{m}$. The effect of $\tilde{r}_2$ on $\tilde{Q}_{tube}$ is also similar to that on $\tilde{m}$. The variation in $\tilde{Q}_{tube}$ due to change in $\tilde{r}_2$ is very small (Fig. 16(b)).

Total heat transfer to the top disc

Total heat transfer to the top disc is a cumulative effect of the local heat fluxes to the disc. Hence it is dependent on the bulk fluid temperature at the exit of the tube and the velocities in the diffuser. It has been seen in the previous sections that the bulk temperature of the fluid in the tube and the fluid velocities are interdependent. For lower fluid velocities in the tube, the fluid temperatures are higher due to diffusion. Higher fluid velocities correspond to a lower bulk temperature at the tube exit.

For a given Gr^*, lower spacing results in a lower mass flow rate. As was seen in Fig. 14, the flux to the top disc near the diffuser entrance is high for low spacing due to higher bulk temperature of the fluid. Further downstream when the fluid temperature falls, the flux comes down rapidly. An increase in spacing causes two opposing effects—a decrease in the bulk temperature at the exit of the tube and an increase in the mass flow rate and hence the heat transfer coefficient in the diffuser. Whether the total heat transfer to the top disc increases or decreases with the spacing depends on which effect is predominant. It can be seen in Fig. 15(c) that for $Gr^* = 5 \times 10^4$, there is a monotonic decrease in heat transfer with an increase in spacing (in the range of the spacings considered), indicating that the decrease in the bulk temperature of the fluid has a greater influence on the heat transfer to the top disc. For $Gr^* = 9 \times 10^2$ and 6×10^3, an increase in spacing is found to cause an initial increase in heat transfer, but a subsequent

increase in spacing results in a decrease in the total heat transfer. This results in an optimal spacing at which the total heat transfer to the vessel is a maximum. At spacings lower than this optimum, reduction in mass flow rate and hence the heat transfer coefficient reduces the heat transfer in the diffuser. On the other hand, for spacings higher than the optimum, lower bulk temperature of the fluid causes a reduction in heat transfer. For $Gr^* = 5 \times 10^4$, no maximum is observed for the investigated range of $\tilde{s}$. It is possible that the optimum value of the spacing is lower than the values considered in the present study.

Since the effect of $\tilde{s}$ on mass flow rate becomes insignificant beyond a certain spacing, the bulk temperature of the fluid at the tube exit also becomes independent of the spacing. This causes the total heat transfer to the top disc to become almost a constant. But in this range of spacing, where mass flow is almost independent of spacing, an increase in spacing should cause a decrease in the fluid velocities in the diffuser due to increase in the area of cross-section. Thus the heat transfer coefficient and hence the total heat transfer to the top disc decrease with spacing as seen in Fig. 15(c).

Increase in the outer radius of the diffuser increases the area available for heat transfer to the top disc. If the fluid temperature at the exit of the diffuser at a given $\tilde{r}_2$ is higher than the top wall temperature, additional area increases the total heat transfer. If the fluid temperature has already reached the top disc temperature, further increase in area will not enhance the heat transfer. This can be seen in Fig. 16(c). For $\tilde{s} = 0.25$ and 0.5, the increase in $\tilde{Q}_{\text{disc}}$ with initial increase in $\tilde{r}_2$ is quite rapid but as the fluid temperature comes down with $\tilde{r}$, further increase in the heat transfer area does not have a significant effect on the total heat transfer.

At smaller spacing ($\tilde{s} = 0.1$), an increase in $\tilde{r}_2$ causes a decrease in the mass flow, reducing the heat transfer coefficient in the diffuser. Due to the opposing effects of the two, i.e. the increase in area and the decrease in the heat transfer coefficient, the total heat transfer corresponding to $\tilde{s} = 0.1$ shows a maximum at a certain value of $\tilde{r}_2$.

5. CONCLUSIONS

Flow visualization and numerical simulation have been conducted on a geometry comprising a vertical hot tube and a radial diffuser. The combination of the buoyancy-induced flow, jet impingement and flow through a radial diffuser shows a strong dependence of flow features on the governing parameters. The results can be summarized as follows.

(i) The studies show a strong dependence of the flow patterns on the diffuser spacing. At low spacings between the diffuser discs, the flow turns from the tube into the diffuser with little separation. An increase in spacing results in a large separation bubble at the sharp bend.

(ii) The mass flow through the system increases with Gr^* as well as the diffuser spacing. At large spacings, an increase in mass flow with further increase in spacing is quite small. The outer radius of the diffuser does not have a strong influence on the mass flow.

(iii) The total heat transfer to the top disc is found to decrease with increase in spacing at high Gr^*. At lower Gr^*, there exists an optimum spacing between the diffuser discs for which the heat transfer to the top disc is a maximum. The increase in outer radius leads to increase in total heat transfer to the disc, particularly at large spacings.

(iv) The flow patterns in the region of bend and the diffuser are found to be similar to those for a forced flow through a similar configuration. However, the flow pattern in the region around the stagnation point and the heat fluxes to the impingement disc show a distinct difference from the case of a forced jet.

The results obtained from this study will be useful in the design of efficient biomass stoves.

REFERENCES

1. W. Elenbaas, The dissipation of heat by free convection from the inner surface of vertical tubes of different shapes of cross-section, *Physica* **9,** 865–874 (1942).
2. J. R. Bodoia and J. F. Osterle, The development of free convection between heated vertical plates, *J. Heat Transfer* **84,** 40–44 (1962).
3. W. Aung, L. S. Fletcher and V. Sernas, Developing laminar free convection between vertical flat plates with asymmetric heating, *Int. J. Heat Mass Transfer* **15,** 2293–2308 (1972).
4. W. Aung, T. J. Kessler and K. I. Beitin, Free convection cooling of electronic systems, *IEEE Trans. Parts, Hybrids, and Packaging* **PHP-9,** 75–86 (1973).
5. H. Akbari and T. R. Borgers, Free convective laminar flow within the Trombe wall channel, *Sol. Energy* **22,** 165–174 (1979).
6. M. Kageyama and R. Izumi, Natural heat convection in a vertical circular tube, *Bull. JSME* **13,** 382–394 (1970).
7. L. P. Davis and J. J. Perona, Development of free convection flow of a gas in a heated vertical open tube, *Int. J. Heat Mass Transfer* **14,** 889–903 (1971).
8. J. R. Dyer, The development of laminar natural convective flow in a vertical uniform heat flux duct, *Int. J. Heat Mass Transfer* **18,** 1455–1465 (1975).
9. T. Fujii, S. Koyama, N. S. Buenconsejo, Jr., Laminar free convection flow rate in a vertical tube, *Int. J. Heat Mass Transfer* **31,** 831–841 (1988).
10. H. S. Mukunda, U. Shrinivasa and S. Dasappa, Portable single-pan woodstoves of high efficiency for domestic use, *Sādhanā* **13,** 237–270 (1988).
11. D. D. Gray and A. Giorgini, The validity of the Boussinesq approximation for liquids and gases, *Int. J. Heat Mass Transfer* **19,** 545–551 (1976).
12. T. Aihara, Effects of inlet boundary conditions on numerical solutions of free convection between vertical parallel plates, *Rep. Inst. High Speed Mech., Tōhoku Univ.* **28** (1973).

13. F. M. White, *Viscous Fluid Flow*, pp. 28–33. McGraw-Hill, New York (1974).
14. B. Gebhart, Y. Jaluria, R. L. Mahajan and B. Sammakia, *Buoyancy-induced Flows and Transport*, pp. 934–936. Hemisphere, New York (1988).
15. S. V. Patankar, *Numerical Heat Transfer and Fluid Flow*. Hemisphere, New York (1980).
16. P. S. Moller, Radial flow without swirl between parallel discs, *Aeronaut. Q.* **14,** 163–186 (1963).
17. N. R. Saad, W. J. M. Douglas and A. S. Mujumdar, Prediction of heat transfer under an axisymmetric laminar impinging jet, *Ind. Engng Chem., Fundam.* **16,** 148–154 (1977).